
Article:
Xu, H. orcid.org/0000-0002-9559-3691, Zeng, G., Liu, W. orcid.org/0000-0003-2968-2888 et al. (1 more author) (2023) MLE-MPPL: a maximum likelihood estimator for multipolarimetric phase linking in MTInSAR. IEEE Transactions on Geoscience and Remote Sensing, 61. 5202913. ISSN 0196-2892

https://doi.org/10.1109/tgrs.2023.3243220

MLE-MPPL: A maximum likelihood estimator for multipolarimetric phase linking in MTInSAR

Huaping Xu, *Member, IEEE*, Guobing Zeng, Wei Liu, *Senior Member, IEEE*, and Yuan Wang

***Abstract*— Multi-Temporal Synthetic Aperture Radar Interferometry (MTInSAR) is an efficient geodetic tool for earth surface displacement measurement, and the polarimetric capability of current and upcoming Synthetic Aperture Radar (SAR) satellites offers a new opportunity to further improve MTInSAR phase series estimation. However, none of existing estimators for multipolarimetric MTInSAR phase series of distributed scatters (DSs) is derived under the minimum root mean square error (RMSE) criterion. In this work, a maximum likelihood estimator for multipolarimetric phase linking (MLE-MPPL) is proposed and the corresponding Cramer-Rao lower bound (CRLB) is also derived by modeling the polarimetric interferometric coherence matrix as the Kronecker product of polarimetric coherence matrix and interferometric coherence matrix. In addition, a new metric called Pol-detR is proposed for performance evaluation of multipolarimetric MTInSAR phase series estimation in practical scenarios where the RMSE is not feasible any more. Experimental results based on both simulated and real data show that the proposed MLE-MPPL achieves the best estimation performance and is more robust against inter-channel interference than existing methods.**

***Index Terms*—Multi-Temporal SAR Interferometry (MTInSAR), multipolarimetric phase linking, CRLB, maximum likelihood estimation.**

I. Introduction

MULTI-TEMPORAL Synthetic Aperture Radar Interferometry (MTInSAR) has become a well-established geodetic mapping tool in the study of earthquakes [1], volcanos [2], landslides [3] [4], and earth surface displacement induced by anthropologic activities [5]. It can characterize centimeter to millimeter level of surface deformation [6]. Thanks to the shorter revisit time and higher image resolution of SAR satellites, much finer deformation monitoring can be achieved in both space and time domains. In the meantime, the multipolarimetric capability of current and upcoming SAR satellites, such as TerraSAR-X/TanDEM-X, Sentinel-1 constellation, Radarsat-2, ALOS-2, BIOMASS, and NISAR, can further enhance the deformation monitoring accuracy and robustness.

A critical problem facing MTInSAR is the decorrelation induced by temporal and spatial baseline, which will hamper accurate estimation of phase series and thereby degrade the deformation monitoring performance. Based on different strategies to handle the decorrelation problem in phase series estimation, MTInSAR techniques can be divided into three classes, which are persistent scatters interferometry (PSI) [7]-[9], Small BAseline Subset (SBAS) [10], and distributed scatters interferometry (DSI) [11]-[15].

PSI identifies persistent scatters (PSs) exhibiting stable amplitude dispersion and performs subsequent phase series analysis on these PSs, thereby avoiding potential performance degradation in the measured displacement field as the decorrelation on PSs is negligible [7]. Hooper developed a Stanford method for persistent scatters [16], which is able to identify more PSs in natural scenes and successfully applied in volcano eruption studies. Many other PSI methods have also been proposed [17]-[19], which mostly differ in their PS selection criteria or displacement field models. However, a main limitation of PSI is its mandatory requirement for PSs, which makes it unsuitable for scenes where PSs are sparse or even nonexistent.

Unlike PSI, SBAS tackles the spatial and temporal decorrelation problem by spatial multilooking and small baseline combination, respectively, and the subsequent phase series estimation is performed on these selected multilooking interferograms through singular value decomposition (SVD). Nevertheless, the multilooking operation inevitably causes loss in resolution. Furthermore, a phase series inconsistency problem was reported in recent studies on SBAS [20] [21].

In DSI, decorrelation of distributed scatters (DSs) is dealt with through adaptive multilooking, which is realized by constructing an interferometric coherence matrix with identified statistical homogeneous pixels (SHPs), and then phase-linking algorithms are applied to estimate the phase series from the constructed interferometric coherence matrix. Under the hypothesis of circular complex gaussian (CCG) distribution, Ferretti *et al* proposed a maximum likelihood phase-linking algorithm [11], i.e., the so-called phase

Manuscript received November 7, 2022. This work was supported by the National Natural Science Foundation of China under the grant of U2241202.

H. Xu, G. Zeng and Y. Wang are with the School of Electronic and Information Engineering, Beihang University, Beijing 100191, China (e-mail: xuhuaping@buaa.edu.cn, zengguobing@buaa.edu.cn, wyuan@buaa.edu.cn).

W. Liu is with the Department of Electronic and Electrical Engineering, University of Sheffield, Sheffield S1 3JD, U.K. (e-mail: w.liu@sheffield.ac.uk).

triangulation algorithm (PTA). Later, Ansari *et al* proposed a more computationally efficient solution [14], which is the eigendecomposition-based maximum-likelihood-estimator of interferometric phase (EMI). Several other phase-linking algorithms like those in CAESAR [12] and PD-PSInSAR [13] have also been proposed.

Through adaptively multilooking and phase-linking, DSI can mitigate the problem of resolution loss and phase inconsistency in SBAS. In the meantime, it improves the phase series estimation accuracy of DSs, thus making up for PSI's weakness. However, all these three techniques are single polarimetric. Additional polarimetric information offered by polarimetric SAR satellites can be exploited to further mitigate the decorrelation problem and achieve more accurate and robust phase series estimation.

Current strategies to apply multipolarimetric data in MTInSAR phase series estimation can be categorized into two types. One is based on polarimetric optimization, and the other is based on interferometric coherence matrix stacking.

The concept of polarimetric differential InSAR optimization in ground base SAR was introduced by selecting the acquisition channel with the highest temporal coherence value in [22]. An exhaustive search polarimetric optimization (ESPO) method was proposed to optimize MTInSAR results under the criterion of amplitude dispersion index (ADI) for PSs or average coherence magnitude for DSs [23] [24]. The suboptimum scattering mechanism [25] method is another option when polarimetric stationarity does not hold. These three methods were then compared systematically using both ground base and orbital data, showing that ESPO can achieve the best performance [26]. In addition, to reduce the huge computational burden of ESPO, coherency matrix decomposition-based PolPSI was proposed as a suboptimal solution [27]. To adaptively identify and process PSs and DSs, a scattering-mechanism-based filtering polarimetric phase OPTimization method was proposed in [28]. In terms of the selection of homogeneous pixels for DSs, Mullissa and Zhao applied the H/A/Alpha-Wishart PolSAR classifier [29]. Apart from ADI and average coherence magnitude, Sadeghi directly employed the temporal coherence, a metric for evaluation of MTInSAR results, as the optimization objective function [30], but it mainly targeted for PSs. Moreover, for multipolarimetric MTInSAR phase series estimation, optimal average coherence does not necessarily indicate the lowest root mean square error (RMSE). Therefore, it cannot guarantee an optimal MTInSAR result, i.e., displacement field. Another polarimetric method for PSs based on maximum likelihood theory constructs the polarimetric likelihood function by assuming the independence of three different polarimetric channels and temporal invariance of decorrelation noise between acquisitions and obtains the optimum deformation and elevation parameters through a time-consuming two-step optimization method [31].

Different from the polarimetric optimization methods, Shen *et al* proposed a total power (TP) coherence matrix construction method [32]-[35], by taking the interferometric coherence matrices of different polarimetric channels as statistical samples and stacking them together to construct a TP coherence matrix. Then, the phase series can be extracted either directly from the off-diagonal elements of the TP coherence matrix [32], or by further employing phase-linking algorithms on the TP coherence matrix [34]. The TP coherence matrix construction method has been proved effective in multipolarimetric phase series estimation [34] [35]; however, by simply stacking the interferometric coherence matrices together, TP is not really the optimal estimator under the hypothesis of CCG distribution.

In pursuit of the optimal solution for multipolarimetric MTInSAR phase series estimation of DSs, a maximum likelihood estimator for multipolarimetric phase linking, hereafter referred to as MLE-MPPL, is proposed in this work and the Cramer-Rao lower bound (CRLB) for multipolarimetric MTInSAR phase series estimation is also derived by modeling the polarimetric interferometric coherence matrix as the Kronecker product of polarimetric coherence matrix and interferometric coherence matrix. Under the hypothesis of CCG distribution, polarimetric stationarity and invariance of decorrelation mechanism among different polarimetric channels, MLE-MPPL is the optimal solution for DSs under the criterion of RMSE and able to asymptotically reach the CRLB. In addition, to further quantitatively evaluate the performance of phase series estimation, a new metric called Pol-detR is proposed as an alternative for RMSE.

The remainder of this paper is organized as follows. In Section II, the maximum likelihood estimation (MLE) for single polarimetric MTInSAR phase series is briefly reviewed. The MLE-MPPL is proposed for multipolarimetric MTInSAR phase series estimation and corresponding CRLB is derived in Section III. Experimental results on both simulated and real data are conducted in Section IV. Conclusions are drawn in Section V.

II. MAXIMUM LIKELIHOOD ESTIMATION FOR SINGLE POLARIMETRIC MTINSAR PHASE SERIES

For a single polarimetric single look complex (SLC) series of N acquisitions $\mathbf{x}=\left[x_1, x_2, \cdots, x_N\right]^T$ that follows the CCG distribution, its probability density function (PDF) is expressed as [11]

$$f\left(\mathbf{x}\right)=\frac{1}{\pi^N \det\left(\mathbf{C}\right)}\exp\{-\mathbf{x}^H\mathbf{C}^{-1}\mathbf{x}\} \tag{1}$$

where $\det\left(\cdot\right)$ denotes the determinant operator, $\mathbf{C}=E\left[\mathbf{x}\mathbf{x}^H\right]$ is the interferometric coherence matrix, $E\left[\cdot\right]$ is the expectation operator and $\left(\cdot\right)^H$ is the Hermitian transpose. $\mathbf{C}$ is modelled as

$$\mathbf{C}=\mathbf{\Theta}^H\mathbf{\Gamma}\mathbf{\Theta} \tag{2}$$

where $\mathbf{\Theta}=\mathrm{diag}\left[\exp(-j\boldsymbol{\theta})\right]$, $\boldsymbol{\theta}=\left[\theta_1, \theta_2, \cdots, \theta_N\right]^T$ includes the phase series to be estimated, and $\mathbf{\Gamma}\in\mathbb{R}^{N\times N}$ is the real-valued coherence matrix. Then, a logarithmic likelihood function can be constructed by the product of P SHPs series

$$L(\boldsymbol{\theta}) = \ln \prod_{k=1}^{P} \frac{1}{\pi^N \det(\mathbf{C})} \exp\{-\mathbf{x}_k^H \mathbf{C}^{-1} \mathbf{x}_k\} \tag{3}$$

where $\mathbf{x}_k$ is the SLC series of the kth SHP. (3) can be formulated in a more compact form as

$$L(\boldsymbol{\theta}) = -\ln\det(\mathbf{C}) - \operatorname{trace}\left(\mathbf{C}^{-1}\hat{\mathbf{C}}\right) \tag{4}$$

where $\operatorname{trace}(\cdot)$ is the trace operator and $\hat{\mathbf{C}} = \frac{1}{P}\sum_{k=1}^{P} \mathbf{x}_k \mathbf{x}_k^H$ is the sample coherence matrix (SCM). By substituting (2) in (4) and eliminating unrelated terms, the likelihood function is rewritten as

$$L(\boldsymbol{\theta}) = -\boldsymbol{\Lambda}^H \left(\boldsymbol{\Gamma}^{-1} \circ \hat{\mathbf{C}}\right) \boldsymbol{\Lambda} \tag{5}$$

where $\circ$ denotes the Hadamard product, and $\boldsymbol{\Lambda} = \exp(-j\boldsymbol{\theta}) = \left[\exp(-j\theta_1), \exp(-j\theta_1), \cdots, \exp(-j\theta_N)\right]^H$. Then, the MLE of phase series $\boldsymbol{\theta}$ can be obtained by maximization of (5), i.e.,

$$\boldsymbol{\theta}_{MLE} = \arg\max_{\boldsymbol{\theta}} -\boldsymbol{\Lambda}^H \left(\boldsymbol{\Gamma}^{-1} \circ \hat{\mathbf{C}}\right) \boldsymbol{\Lambda} \tag{6}$$

Two approaches can be employed to solve this optimization problem. One is the iterative PTA method proposed in [11], which uses the computationally expensive Broyden–Fletcher–Goldfarb–Shanno algorithm. The other is EMI [14], which is more efficient by performing eigenvalue decomposition of $\boldsymbol{\Gamma}^{-1} \circ \hat{\mathbf{C}}$ and then taking the eigenvector corresponding to the smallest eigenvalue as the solution. It should be noted that the coherence matrix $\boldsymbol{\Gamma}$ is unknown and thus needs to be estimated. A widely used estimation for the coherence matrix is $\hat{\boldsymbol{\Gamma}} = \left|\hat{\mathbf{C}}\right|$, where $|\cdot|$ is the modulus operator.

III. MLE-MPPL AND CRLB

In polarimetric SAR, the Sinclair backscattering matrix

$$S = \begin{bmatrix} S_{HH} & S_{HV} \\ S_{VH} & S_{VV} \end{bmatrix} \tag{7}$$

can be fully represented by a Pauli basis scattering vector as [23]

$$\mathbf{k} = \left[\frac{1}{\sqrt{2}} S_{HH+VV}, \frac{1}{\sqrt{2}} S_{HH-VV}, \sqrt{2} S_{HV}\right]^T \tag{8}$$

where the cross-polar reciprocity $S_{HV} = S_{VH}$ is assumed.

ESPO is a typical optimal polarimetric optimization method, and searches for an optimum projection vector $\boldsymbol{\omega}_{opt}$ through maximization of the average coherence magnitude [24]

$$\boldsymbol{\omega}_{opt} = \arg\max_{\boldsymbol{\omega}} \frac{2}{(N-1)N} \sum_{i=1}^{N}\sum_{j>i}^{N} \left| \frac{\boldsymbol{\omega}^H \boldsymbol{\Omega}_{ij} \boldsymbol{\omega}}{\sqrt{\boldsymbol{\omega}^H \mathbf{T}_{ii} \boldsymbol{\omega}} \sqrt{\boldsymbol{\omega}^H \mathbf{T}_{jj} \boldsymbol{\omega}}} \right| \tag{9}$$

where $\mathbf{T}_{ii} = E\left[\mathbf{k}_i \mathbf{k}_i^H\right]$, $\boldsymbol{\Omega}_{ij} = E\left[\mathbf{k}_i \mathbf{k}_j^H\right]$ and $\mathbf{k}_i$ is the Pauli basis scattering vector of the ith acquisition. The polarimetric stationarity is often assumed in the optimization of (9). By projecting the multipolarimetric data onto $\boldsymbol{\omega}_{opt}$, an optimum polarimetric channel $\mu = \boldsymbol{\omega}_{opt}^H \mathbf{k}$ is obtained. Subsequent phase-linking operation described in Section II is then applied on the optimum channel to estimate the phase series. However, for DSs, an optimal average coherence magnitude achieved by ESPO cannot guarantee the best phase series estimation with the lowest RMSE.

The TP method considers the interferometric coherence matrix of different polarimetric channels as statistical samples and adds them up to construct a TP matrix, which can be expressed as

$$\mathbf{C}_{TP} = \sum_{i=1}^{3} \mathbf{C}_i \tag{10}$$

where $\mathbf{C}_i$ stands for the interferometric coherence matrix of the ith channel in Pauli basis. Then, the phase series is acquired by replacing $\boldsymbol{\Gamma}$ and $\hat{\mathbf{C}}$ in (6) with $\left|\mathbf{C}_{TP}\right|$ and $\mathbf{C}_{TP}$ respectively. Nevertheless, it is still not the optimal solution under the hypothesis of CCG distribution.

In this section, the MLE for multipolarimetric MTInSAR phase series estimation, MLE-MPPL, is derived under three hypotheses: CCG, polarimetric stationarity and invariance of decorrelation mechanism among different polarimetric channels. The latter two hypotheses are already applied in ESPO and TP respectively. The likelihood function for multipolarimetric MTInSAR phase series estimation is constructed and MLE-MPPL is obtained by modeling the polarimetric interferometric coherence matrix as the Kronecker product of polarimetric coherence matrix and interferometric coherence matrix. Furthermore, the CRLB for multipolarimetric MTInSAR phase series estimation is also derived by referring to the single polarimetric scenario.

A. MLE-MPPL

Similar to the single polarimetric case in (1), for a fully polarimetric SLC series of N acquisitions $\mathbf{y}$ following CCG distribution, its PDF can be written as

$$f(\mathbf{y}) = \frac{1}{\pi^N \det(\mathbf{T})} \exp\{-\mathbf{y}^H \mathbf{T}^{-1} \mathbf{y}\} \tag{11}$$

where $\mathbf{T} = E\left[\mathbf{y}\mathbf{y}^H\right]$ is the polarimetric interferometric coherence matrix, and $\mathbf{y} = \left[\mathbf{K}_1^T, \mathbf{K}_2^T, \mathbf{K}_3^T\right]^T$, with

$$\mathbf{K}_i = \left[x_1^i, x_2^i, \cdots, x_N^i\right]^T, i = 1,2,3 \tag{12}$$

where $x_j^i, j = 1,2,\cdots,N$ is the jth SLC of the ith channel in Pauli basis. Like in (3), a logarithmic multipolarimetric likelihood function can be constructed as

$$L_{pol}\left(\boldsymbol{\theta}\right)=\ln\prod_{k=1}^{P}\frac{1}{\pi^{N}\det\left(\mathbf{T}\right)}\exp\{-\mathbf{y}_{k}^{H}\mathbf{T}^{-1}\mathbf{y}_{k}\} \tag{13}$$

where P is the SHPs number. (13) can be further expanded as

$$L_{pol}\left(\boldsymbol{\theta}\right)=-P\ln\det\left(\mathbf{T}\right)-\sum_{k=1}^{P}\mathbf{y}_{k}^{H}\mathbf{T}^{-1}\mathbf{y}_{k}-NP\ln\pi \tag{14}$$

Replacing the second term in (14) with its trace and using the trace property, it follows that

$$L_{pol}\left(\boldsymbol{\theta}\right)=-P\ln\det\left(\mathbf{T}\right)-\operatorname{trace}\left(\sum_{k=1}^{P}\mathbf{T}^{-1}\mathbf{y}_{k}\mathbf{y}_{k}^{H}\right)-NP\ln\pi \tag{15}$$

Eliminating the constant terms and constant factor, (15) can be formulated in a more compact form,

$$L_{pol}\left(\boldsymbol{\theta}\right)=-\ln\det\left(\mathbf{T}\right)-\operatorname{trace}\left(\mathbf{T}^{-1}\hat{\mathbf{T}}\right) \tag{16}$$

where $\hat{\mathbf{T}}=\frac{1}{P}\sum_{k=1}^{P}\mathbf{y}_{k}\mathbf{y}_{k}^{H}$ can be interpreted as the sample polarimetric interferometric coherence matrix (SPCM). Now the multipolarimetric likelihood function in (16) takes a similar form as the single polarimetric one in (4). Therefore, to achieve the MLE, the polarimetric interferometric coherence matrix $\mathbf{T}$ has to be further analyzed.

Given the polarimetric stationarity and invariance of decorrelation mechanism among different polarimetric channels [36], $\mathbf{T}$ can be modelled as

$$\mathbf{T}=\mathbf{C}_{pol}\otimes\mathbf{C}_{coh} \tag{17}$$

by assuming an equal scattering mechanism (ESM), where $\otimes$ denotes the Kronecker product, $\mathbf{C}_{pol}\in\mathbb{C}^{3\times3}$ and $\mathbf{C}_{coh}\in\mathbb{C}^{N\times N}$ are the polarimetric coherence matrix and interferometric coherence matrix corresponding to the ESM, respectively. In order to relate $\mathbf{T}$ with the phase series to be estimated, $\mathbf{C}_{coh}$ can be further modelled as in (2), which is

$$\mathbf{C}_{coh}=\boldsymbol{\Theta}^{H}\boldsymbol{\Gamma}_{ESM}\boldsymbol{\Theta} \tag{18}$$

where $\boldsymbol{\Gamma}_{ESM}$ is the real-valued interferometric coherence matrix corresponding to the ESM.

According to [37], the SPCM $\hat{\mathbf{T}}$ can be decomposed by the sum of a set of kronecker products as

$$\hat{\mathbf{T}}=\sum_{i=1}^{3\times3}\tilde{\mathbf{C}}_{pol,i}\otimes\tilde{\mathbf{C}}_{coh,i} \tag{19}$$

where $\tilde{\mathbf{C}}_{pol,i}\in\mathbb{C}^{3\times3}$ and $\tilde{\mathbf{C}}_{coh,i}\in\mathbb{C}^{N\times N}$. This operation is called sum of kronecker product (SKP) decomposition [36].

Substituting (17)-(19) into (16), the multipolarimetric likelihood function $L_{pol}\left(\boldsymbol{\theta}\right)$ can be transformed into

$$\begin{aligned}L_{pol}\left(\boldsymbol{\theta}\right)&=-\ln\det\left(\mathbf{C}_{pol}\otimes\left(\boldsymbol{\Theta}^{H}\boldsymbol{\Gamma}_{ESM}\boldsymbol{\Theta}\right)\right)\\&-\sum_{i=1}^{3\times3}\operatorname{trace}\left(\left(\mathbf{C}_{pol}\otimes\left(\boldsymbol{\Theta}^{H}\boldsymbol{\Gamma}_{ESM}\boldsymbol{\Theta}\right)\right)^{-1}\left(\tilde{\mathbf{C}}_{pol,i}\otimes\tilde{\mathbf{C}}_{coh,i}\right)\right)\end{aligned} \tag{20}$$

Before performing further analysis on (20), some properties of Kronecker product need to be reviewed. Let $\mathbf{A}\in\mathbb{C}_{m\times m}$, $\mathbf{B}\in\mathbb{C}_{n\times n}$, $\mathbf{M}\in\mathbb{C}_{m\times m}$, $\mathbf{N}\in\mathbb{C}_{n\times n}$. The following properties for Kronecker product hold.

Determinant property:

$$\det\left(\mathbf{A}\otimes\mathbf{B}\right)=\det\left(\mathbf{A}\right)^{n}\det\left(\mathbf{B}\right)^{m} \tag{21}$$

Inverse property: if $\mathbf{A}$ and $\mathbf{B}$ are full rank,

$$\left(\mathbf{A}\otimes\mathbf{B}\right)^{-1}=\mathbf{A}^{-1}\otimes\mathbf{B}^{-1} \tag{22}$$

Trace property:

$$\operatorname{trace}\left(\mathbf{A}\otimes\mathbf{B}\right)=\operatorname{trace}\left(\mathbf{A}\right)\operatorname{trace}\left(\mathbf{B}\right) \tag{23}$$

Mixed-product property:

$$\left(\mathbf{A}\otimes\mathbf{B}\right)\left(\mathbf{M}\otimes\mathbf{N}\right)=\left(\mathbf{AM}\right)\otimes\left(\mathbf{BN}\right) \tag{24}$$

According to the determinant and inverse properties, (20) is transformed into

$$\begin{aligned}L_{pol}\left(\boldsymbol{\theta}\right)&=-3\ln\det\left(\boldsymbol{\Gamma}_{ESM}\right)-N\ln\det\left(\mathbf{C}_{pol}\right)\\&-\sum_{i=1}^{3\times3}\operatorname{trace}\left(\left(\mathbf{C}_{pol}^{-1}\otimes\left(\boldsymbol{\Theta}^{H}\boldsymbol{\Gamma}_{ESM}^{-1}\boldsymbol{\Theta}\right)\right)\left(\tilde{\mathbf{C}}_{pol,i}\otimes\tilde{\mathbf{C}}_{coh,i}\right)\right)\end{aligned} \tag{25}$$

Exploiting the mixed-product and trace properties, (25) is rewritten as

$$\begin{aligned}L_{pol}\left(\boldsymbol{\theta}\right)&=-\sum_{i=1}^{3\times3}\operatorname{trace}\left(\mathbf{C}_{pol}^{-1}\tilde{\mathbf{C}}_{pol,i}\right)\operatorname{trace}\left(\boldsymbol{\Theta}^{H}\boldsymbol{\Gamma}_{ESM}^{-1}\boldsymbol{\Theta}\tilde{\mathbf{C}}_{coh,i}\right)\\&-3\ln\det\left(\boldsymbol{\Gamma}_{ESM}\right)-N\ln\det\left(\mathbf{C}_{pol}\right)\end{aligned} \tag{26}$$

Eliminating the terms unrelated to $\boldsymbol{\theta}$, (26) becomes

$$L_{pol}\left(\boldsymbol{\theta}\right)=-\sum_{i=1}^{3\times3}\operatorname{trace}\left(\mathbf{C}_{pol}^{-1}\tilde{\mathbf{C}}_{pol,i}\right)\operatorname{trace}\left(\boldsymbol{\Theta}^{H}\boldsymbol{\Gamma}_{ESM}^{-1}\boldsymbol{\Theta}\tilde{\mathbf{C}}_{coh,i}\right) \tag{27}$$

Then, the MLE-MPPL of $\boldsymbol{\theta}$ can be obtained from (26) as

$$\boldsymbol{\theta}_{MLE-MPPL}=\arg\max_{\boldsymbol{\theta}}-\boldsymbol{\Lambda}^{H}\left(\sum_{i=1}^{3\times3}\operatorname{trace}\left(\mathbf{C}_{pol}^{-1}\tilde{\mathbf{C}}_{pol,i}\right)\left(\boldsymbol{\Gamma}_{ESM}^{-1}\circ\tilde{\mathbf{C}}_{coh,i}\right)\right)\boldsymbol{\Lambda} \tag{28}$$

Finally, by performing eigenvalue decomposition of $\sum_{i=1}^{3\times3}\operatorname{trace}\left(\mathbf{C}_{pol}^{-1}\tilde{\mathbf{C}}_{pol,i}\right)\left(\boldsymbol{\Gamma}_{ESM}^{-1}\circ\tilde{\mathbf{C}}_{coh,i}\right)$ and taking the eigenvector corresponding to the minimum eigenvalue as the solution, the proposed MLE-MPPL is completed.

Note that in (28) $\tilde{\mathbf{C}}_{pol,i}$ and $\tilde{\mathbf{C}}_{coh,i}$ can be directly acquired by performing SKP decomposition on the SPCM, whereas the polarimetric coherence matrix $\mathbf{C}_{pol}$ and coherence matrix $\boldsymbol{\Gamma}_{ESM}$ are unknown and thus need to be estimated.

Under the hypothesis of polarimetric stationarity, the

polarimetric coherence matrix $\mathbf{C}_{pol}$ can be estimated by

$$\hat{\mathbf{C}}_{pol} = \frac{1}{N}\sum_{i=1}^{N}\mathbf{k}_i\mathbf{k}_i^H \tag{29}$$

The estimation of coherence matrix $\mathbf{\Gamma}_{ESM}$ in multipolarimetric scenario is different from that in the single polarimetric scenario. Given ESM and invariance of decorrelation mechanism among different polarimetric channels, a reasonable estimation of coherence matrix $\mathbf{\Gamma}_{ESM}$ can be achieved by averaging the interferometric coherence matrices of three different polarimetric channels, given by

$$\hat{\mathbf{\Gamma}}_{ESM} = \left|\frac{1}{3}\sum_{i=1}^{3}\hat{\mathbf{C}}_i\right| \tag{30}$$

where $\hat{\mathbf{C}}_i$ is the SCM of the *i*th polarimetric channel in Pauli basis. As suggested in [36], to calibrate the unbalanced backscattered signal power among different tracks and polarimetric channels, a normalization operation is recommended. Therefore, $\hat{\mathbf{T}}$, $\hat{\mathbf{C}}_{pol}$ and $\hat{\mathbf{C}}_i$ are normalized as in [36] before they are employed in MLE-MPPL.

From (6), (10) and (28), a noteworthy inherent relationship between TP and the proposed MLE-MPPL can be found that TP is equivalent to MLE-MPPL when the polarimetric coherence matrix $\mathbf{C}_{pol}$ is an identity matrix. However, since $\mathbf{C}_{pol}$ is unlikely to be an identity matrix in practice [44], MLE-MPPL is more effective in general than TP.

In summary, the flowchart of MLE-MPPL is shown in Fig. 1. First, the SKP decomposition is performed on the SPCM as in (19) to obtain $\tilde{\mathbf{C}}_{pol,i}$ and $\tilde{\mathbf{C}}_{coh,i}$; the polarimetric coherence matrix and interferometric coherence matrix are estimated through (29) and (30) respectively; then, substitute $\tilde{\mathbf{C}}_{pol,i}$, $\tilde{\mathbf{C}}_{coh,i}$, $\hat{\mathbf{C}}_{pol}$ and $\hat{\mathbf{\Gamma}}_{ESM}$ into (28) and solve the optimization problem to acquire the multipolarimetric MTInSAR phase series.

B. CRLB for multipolarimetric MTInSAR phase series estimation

The CRLB for single polarimetric MTInSAR phase series estimation has already been derived in [38] [39]. Here, we derive the CRLB for fully polarimetric MTInSAR phase series estimation with the model described in (16).

According to [40], the Fisher information matrix (FIM) for the fully polarimetric phase series estimation can be expressed as

$$\left(\mathbf{J}\right)_{ij} = \mathrm{trace}\left(\mathbf{T}^{-1}\frac{\partial\mathbf{T}}{\partial\theta_i}\mathbf{T}^{-1}\frac{\partial\mathbf{T}}{\partial\theta_j}\right) \tag{31}$$

where $\left(\mathbf{J}\right)_{ij}$ denotes the element of FIM $\mathbf{J}$ at the *i*th row and the *j*th column. Substituting (17) into (31), we have

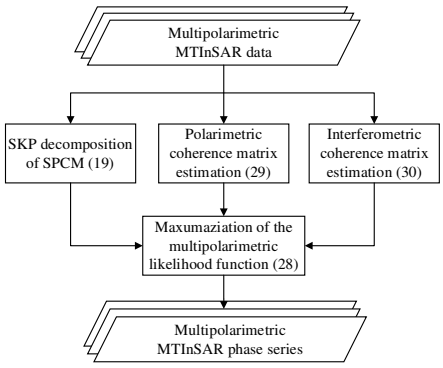

Fig. 1. Flowchart of the proposed MLE-MPPL.

$$\left(\mathbf{J}\right)_{ij} = \mathrm{trace}\left(\left(\mathbf{C}_{pol}\otimes\mathbf{C}_{coh}\right)^{-1}\frac{\partial\left(\mathbf{C}_{pol}\otimes\mathbf{C}_{coh}\right)}{\partial\theta_i}\left(\mathbf{C}_{pol}\otimes\mathbf{C}_{coh}\right)^{-1}\frac{\partial\left(\mathbf{C}_{pol}\otimes\mathbf{C}_{coh}\right)}{\partial\theta_j}\right) \tag{32}$$

Considering the differential property of Kronecker product

$$d\left(\mathbf{A}\otimes\mathbf{B}\right) = \left(d\mathbf{A}\right)\otimes\mathbf{B} + \mathbf{A}\otimes\left(d\mathbf{B}\right) \tag{33}$$

(32) can be further transformed into

$$\left(\mathbf{J}\right)_{ij} = \mathrm{trace}\left(\left(\mathbf{C}_{pol}\otimes\mathbf{C}_{coh}\right)^{-1}\left(\mathbf{C}_{pol}\otimes\frac{\partial\mathbf{C}_{coh}}{\partial\theta_i}+\mathbf{C}_{coh}\otimes\frac{\partial\mathbf{C}_{pol}}{\partial\theta_i}\right)\left(\mathbf{C}_{pol}\otimes\mathbf{C}_{coh}\right)^{-1}\left(\mathbf{C}_{pol}\otimes\frac{\partial\mathbf{C}_{coh}}{\partial\theta_j}+\mathbf{C}_{coh}\otimes\frac{\partial\mathbf{C}_{pol}}{\partial\theta_j}\right)\right) \tag{34}$$

As $\mathbf{C}_{pol}$ is not related to $\boldsymbol{\theta}$, using the inverse property, (34) can be simplified as

$$\left(\mathbf{J}\right)_{ij} = \mathrm{trace}\left(\left(\mathbf{C}_{pol}^{-1}\otimes\mathbf{C}_{coh}^{-1}\right)\left(\mathbf{C}_{pol}\otimes\frac{\partial\mathbf{C}_{coh}}{\partial\theta_i}\right)\left(\mathbf{C}_{pol}^{-1}\otimes\mathbf{C}_{coh}^{-1}\right)\left(\mathbf{C}_{pol}\otimes\frac{\partial\mathbf{C}_{coh}}{\partial\theta_j}\right)\right) \tag{35}$$

Applying the mix-product property, (35) becomes

$$\begin{aligned}\left(\mathbf{J}\right)_{ij} &= \mathrm{trace}\left(\left(\mathbf{C}_{pol}^{-1}\mathbf{C}_{pol}\right)\otimes\left(\mathbf{C}_{coh}^{-1}\frac{\partial\mathbf{C}_{coh}}{\partial\theta_i}\right)\left(\mathbf{C}_{pol}^{-1}\mathbf{C}_{pol}\right)\otimes\left(\mathbf{C}_{coh}^{-1}\frac{\partial\mathbf{C}_{coh}}{\partial\theta_j}\right)\right)\\ &= \mathrm{trace}\left(\left(\mathbf{I}_{3\times3}\mathbf{I}_{3\times3}\right)\otimes\left(\mathbf{C}_{coh}^{-1}\frac{\partial\mathbf{C}_{coh}}{\partial\theta_i}\mathbf{C}_{coh}^{-1}\frac{\partial\mathbf{C}_{coh}}{\partial\theta_j}\right)\right)\end{aligned} \tag{36}$$

where $\mathbf{I}_{3\times3}$ is the 3×3 identity matrix. Then, according to the trace property of Kronecker product, (36) can be further transformed into

$$\begin{aligned}\left(\mathbf{J}\right)_{ij} &= \mathrm{trace}\left(\mathbf{I}_{3\times3}\right)\mathrm{trace}\left(\mathbf{C}_{coh}^{-1}\frac{\partial\mathbf{C}_{coh}}{\partial\theta_i}\mathbf{C}_{coh}^{-1}\frac{\partial\mathbf{C}_{coh}}{\partial\theta_j}\right)\\ &= 3\mathrm{trace}\left(\mathbf{C}_{coh}^{-1}\frac{\partial\mathbf{C}_{coh}}{\partial\theta_i}\mathbf{C}_{coh}^{-1}\frac{\partial\mathbf{C}_{coh}}{\partial\theta_j}\right)\end{aligned} \tag{37}$$

where $\mathrm{trace}\left(\mathbf{C}_{coh}^{-1}\frac{\partial\mathbf{C}_{coh}}{\partial\theta_i}\mathbf{C}_{coh}^{-1}\frac{\partial\mathbf{C}_{coh}}{\partial\theta_j}\right)$ is exactly the element of FIM for single polarimetric MTInSAR phase series estimation at the ith row and the jth column. Therefore, the relationship between the FIMs of single and fully polarimetric scenarios can be derived

$$\mathbf{J} = 3\mathbf{J}_{\mathrm{single}} \tag{38}$$

where $\mathbf{J}_{\mathrm{single}}$ is single polarimetric FIM. From (38), it can be found that the CRLB for fully polarimetric phase series estimation is $1/3$ that of the single polarimetric scenario.

IV. Numerical results

In this section, a new metric called Pol-detR for performance evaluation of multipolarimetric MTInSAR phase series estimation is firstly proposed. Then, phase estimation is conducted on both one-dimensional and two-dimensional synthetic data generated through the Monte Carlo method [41], by considering an extended Bragg scattering model for polarimetric coherence matrix and two different decorrelation models for interferometric coherence matrix [32]. Through experiments on data generated at different inter-channel interference level, the robustness of MLE-MPPL against inter-channel interference is verified. In addition, the validity of the new metric Pol-detR is also shown by exploring its relationship with RMSE. Finally, real data experiments are conducted on 30 dual polarimetric VV-VH Sentinel-1A Interferometric Wide swath SLC images to further demonstrate the performance of the proposed MLE-MPPL method.

A. Pol-detR: a new metric to evaluate the performance of multipolarimetric MTInSAR phase series estimation

The RMSE of the estimated phase series with respect to its true value can perfectly describe the accuracy of estimation. However, it is not applicable in practice as the true phase series value is unknown. Therefore, pseudo coherence [42] and residue points [43] are often used in a real situation, which only reflects the spatial phase quality of interferograms constructed by the estimated phase series. To complement the currently limited metrics, a new metric called Pol-detR is proposed.

Inspired by the detR metric proposed in [15] for single polarimetric MTInSAR phase series estimation, Pol-detR is defined as the likelihood value of a certain solution, which is expressed as

$$\text{Pol-detR} = \sum_{i=1}^{3\times3}\mathrm{trace}\left(\mathbf{C}_{pol}^{-1}\tilde{\mathbf{C}}_{pol,i}\right)\mathrm{trace}\left(\hat{\mathbf{\Theta}}\tilde{\mathbf{C}}_{coh,i}\hat{\mathbf{\Theta}}^{H}\mathbf{\Gamma}_{MLE}^{-1}\right) + 3\ln\left|\mathbf{\Gamma}_{MLE}^{-1}\right| \tag{39}$$

where $\hat{\mathbf{\Theta}}$ is constructed by the estimated phase series and $\mathbf{\Gamma}_{MLE}$ is the MLE of interferometric coherence matrix $\mathbf{\Gamma}_{ESM}$, which has been derived as

$$\mathbf{\Gamma}_{MLE} = \frac{1}{3}\sum_{i=1}^{3\times3}\mathrm{trace}\left(\mathbf{C}_{pol}^{-1}\tilde{\mathbf{C}}_{pol,i}\right)\mathrm{Re}\left(\hat{\mathbf{\Theta}}\tilde{\mathbf{C}}_{coh,i}\hat{\mathbf{\Theta}}^{H}\right) \tag{40}$$

where $\mathrm{Re}(\cdot)$ denotes the real part of its complex argument. Detailed derivation of $\mathbf{\Gamma}_{MLE}$ can be found in appendix A. By replacing the coherence matrix $\mathbf{\Gamma}_{ESM}$ with its MLE $\mathbf{\Gamma}_{MLE}$, Pol-detR represents a more accurate likelihood value for a given solution, and it can be seen as a goodness-of-fit index between the observed data and estimation result under the CCG model.

B. Experiments on simulated multipolarimetric MTInSAR data

To evaluate the performance of the proposed MLE-MPPL, Monte Carlo method [41] is employed to simulate multipolarimetric MTInSAR data. As shown in (17), the polarimetric interferometric coherence matrix is modelled as the Kronecker product of polarimetric coherence matrix and interferometric coherence matrix. Therefore, their simulation models are discussed separately.

For the polarimetric coherence matrix, an extended Bragg scattering model [44] is considered, which is

$$\mathbf{C}_{pol} = \begin{bmatrix} C_1 & C_2\mathrm{sinc}\left(2\beta_1\right) & 0 \\ C_2^{*}\mathrm{sinc}\left(2\beta_1\right) & C_3\left(1+\mathrm{sinc}\left(4\beta_1\right)\right) & 0 \\ 0 & 0 & C_3\left(1-\mathrm{sinc}\left(4\beta_1\right)\right) \end{bmatrix} \tag{41}$$

where $C_1 = 1.0, C_2 = 0.2+0.2i, C_3 = 0.5$ and $\beta_1 = 0.05\pi$.

As in (18), the interferometric coherence matrix can be fully represented by the phase series $\boldsymbol{\theta}$ and real-valued coherence matrix $\mathbf{\Gamma}_{ESM}$. Considering a general decorrelation model [14]

$$\left(\mathbf{\Gamma}_{ESM}\right)_{ij} = \left(\gamma_0-\gamma_\infty\right)\exp\left(-\delta t_{ij}/\tau\right)+\gamma_\infty \tag{42}$$

where δt_{ij} denotes the temporal baseline between the ith and jth acquisition, τ is a constant which reflects the extent to which the decorrelation increases with the temporal baseline. γ_0 and γ_∞ are initial coherence and long-term coherence values, respectively. When $\gamma_\infty = 0$, (42) is referred to as the *exponential decay* model, and $\gamma_\infty \neq 0$ indicates a *long-term coherence* model. In this simulation, both decorrelation models are applied by setting $\gamma_0 = 0.6, \gamma_\infty = 0$ for *exponential decay* and $\gamma_0 = 0.6, \gamma_\infty = 0.2$ for *long-term coherence*, respectively. τ is set to be 50 days, and the temporal sampling interval τ_0 is

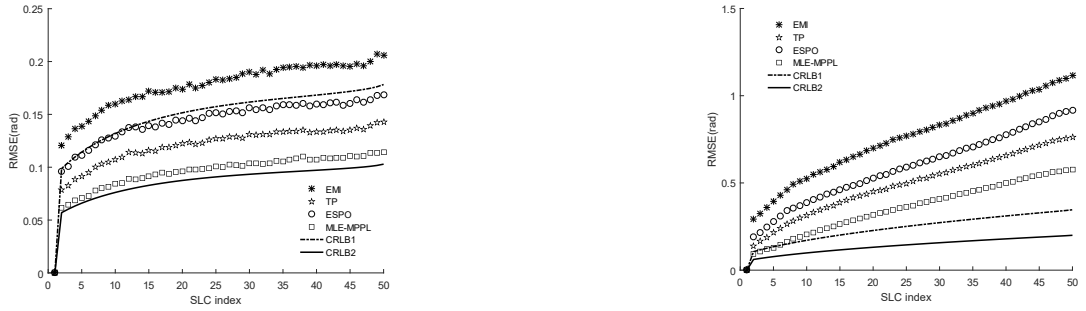

(a) (b)

Fig. 2. RMSEs of different methods: (a) *long-term coherence* decorrelation model; (b) *exponential decay* decorrelation model.

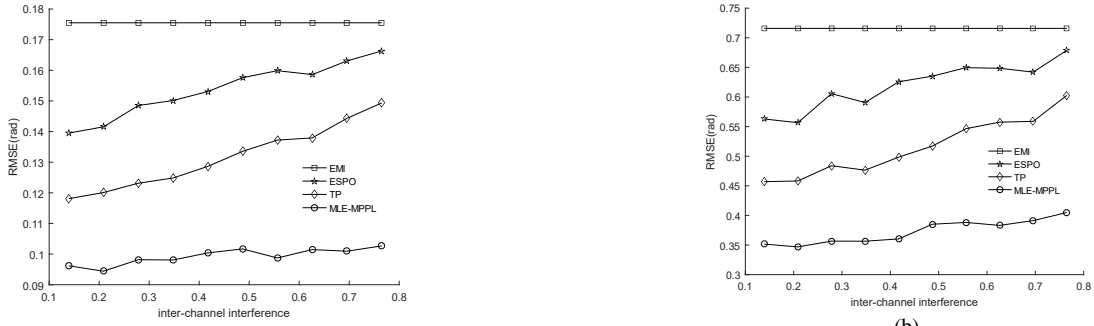

(a) (b)

Fig. 3. RMSEs of four methods with different inter-channel interference level: (a) *long-term coherence* decorrelation model; (b) *exponential decay* decorrelation model.

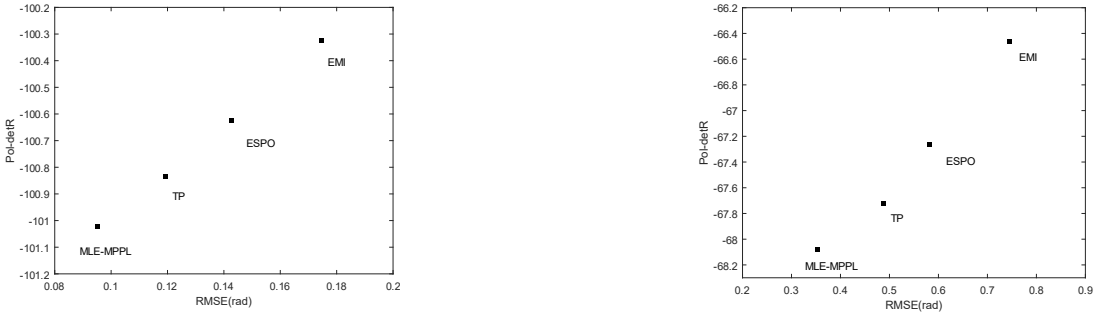

(a) (b)

Fig. 4. Relationship between RMSE and Pol-detR: (a) *long-term coherence* decorrelation model; (b) *exponential decay* decorrelation model.

identical to the configuration of Sentinel-1A/B constellation, which is 6 days.

The phase series $\boldsymbol{\theta}$ is generated by applying a 1 mm/year deformation velocity and temporal sampling interval $\tau_0 = 6$ days. Note that the random atmospheric delay and orbit error signals are ignored here to ensure the stationarity of simulated CCG data [14]. A series of 50 fully polarimetric SLC images are simulated with 300 independent samples, and 2000 realizations are implemented to evaluate the RMSE of the estimated phase series $\hat{\boldsymbol{\theta}}$ of different methods.

To further demonstrate the advantage of the proposed MLE-MPPL, a two-dimensional phase series $\boldsymbol{\theta}_{2D}$ is generated by a Gaussian function as in [35]. And a series of 50 fully polarimetric 101×101 SLC images are simulated in the *long-term coherence* decorrelation model.

1) Result analysis for one-dimensional data

Phase series estimation on the one-dimensional simulated data is conducted with four different methods, i.e., single polarimetric EMI [14], ESPO [24], TP [32] and the proposed MLE-MPPL. ESPO is implemented with additional EMI phase-linking operation on the optimal polarimetric channel and the searching step size for the parameter group $(\alpha, \beta, \delta, \varphi)$ is set to $(5^\circ, 5^\circ, 5^\circ, 5^\circ)$. In the TP method, the phase series is also extracted by applying EMI phase-linking to the TP matrix. The RMSEs of four methods in *long-term coherence* model and *exponential decay* model are shown in Fig. 2(a) and 2(b), respectively. In addition, the CRLB of single polarimetric phase series estimation CRLB1 and fully polarimetric phase series

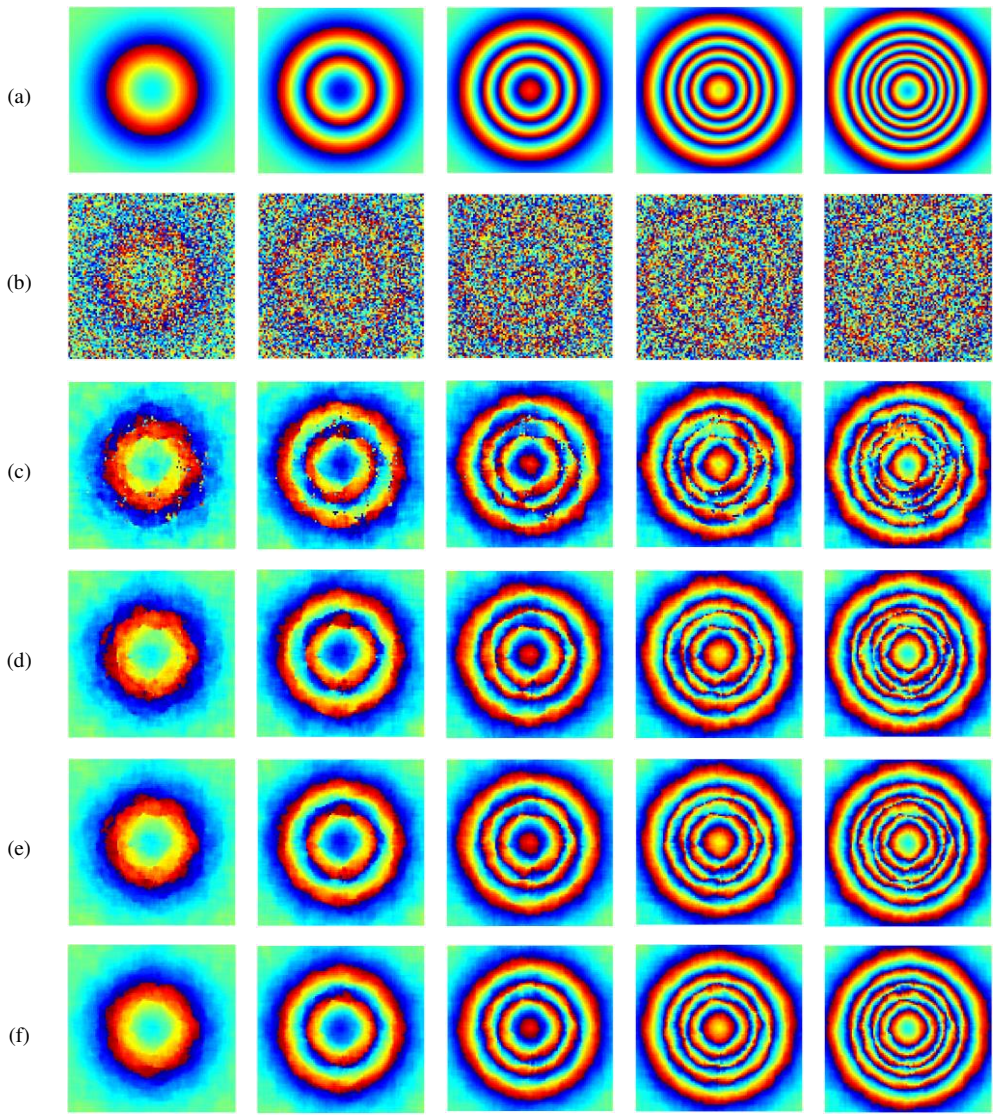

Fig. 5. Interferograms of the 1st and ith images, $i = 10, 20, 30, 40, 50$ respectively (left to right) by each method: (a) reference; (b) original VV; (c) EMI; (d) ESPO; (e) TP; (f) MLE-MPPL.

TABLE I
AVERAGE RMSE BY FOUR METHODS

Method	EMI	ESPO	TP	MLE-MPPL
Average RMSE (rad)	0.4051	0.3706	0.3141	0.2525

estimation CRLB2 are also plotted in Fig. 2.

From Fig. 2(a) and 2(b), it can be observed that the single polarimetric EMI presents much larger RMSE than the other three fully polarimetric methods. Among three fully polarimetric methods, ESPO has the largest RMSE, whereas the proposed MLE-MPPL outperforms the other two methods with the minimum RMSE at all SLCs. Besides, its RMSE curve is the closest to the corresponding CRLB in both *long-term coherence* and *exponential decay* models. The gap between the CRLB and MLE-MPPL is due to errors induced by the biased estimation of $\mathbf{\Gamma}_{ESM}$ and $\mathbf{C}_{pol}$ as in (29) and (30).

2) Investigation of the influence induced by inter-channel interference on the estimation accuracy

As mentioned in [32] [34], the inter-channel interference can degrade the accuracy of phase series estimation. To investigate its effect on the proposed method, a set of experiments at different levels of inter-channel interference are conducted.

In the polarimetric coherence matrix of the extended Bragg scattering model, the off-diagonal elements, such as the correlation coefficient $\left|C_2 \mathrm{sinc}\left(2\beta_1\right)\right|$, indicate the level of inter-channel interference between different polarimetric channels. A higher $\left|C_2 \mathrm{sinc}\left(2\beta_1\right)\right|$ indicates a higher level of

inter-channel interference. A set of multipolarimetric MTInSAR data are simulated by setting different $\left|C_2\mathrm{sinc}\left(2\beta_1\right)\right|$. EMI, ESPO, TP and MLE-MPPL are applied to these data, and the resultant RMSEs are shown in Fig. 3(a) and 3(b). It can be found that the RMSE of EMI is not affected by the inter-channel interference level because EMI is a single polarimetric method. As for fully polarimetric methods, the increase of inter-channel interference level leads to the increase of RMSE for ESPO and TP in both decorrelation models, resulting in degradation of estimation accuracy. For MLE-MPPL, its RMSE basically remains unchanged in the *long-term coherence* model, while in the *exponential decay* model, the RMSE curve of MLE-MPPL increases more slowly than those of ESPO and TP. In summary, MLE-MPPL is more robust than ESPO and TP against the inter-channel interference.

3) Verification of the new metric: Pol-detR

To demonstrate the effectiveness of the newly proposed metric, the Pol-detR and RMSE of the estimated phase series acquired by four methods are compared. The average RMSE and Pol-detR values of four methods with two different decorrelation models are illustrated in Fig. 4. It is shown that Pol-detR monotonically increases with the increase of RMSE in both decorrelation models. Thus, a lower Pol-detR value indicates a lower RMSE and a higher estimation accuracy. Therefore, Pol-detR can serve as an alternative metric for real data processing when the RMSE is not applicable.

4) Result analysis for two-dimensional data

EMI, ESPO, TP and MLE-MPPL are applied to the two-dimensional simulated data respectively [35], with the window size for estimation of interferometric coherence matrix and polarimetric interferometric coherence matrix being 9×9. Interferograms constructed by the estimated phase series of these four methods are shown in Fig. 5 and they are constructed by the first and the *i*th images, where $i=10,20,30,40,50$, respectively (left to right). The average RMSEs by the four methods are listed in Table I. It can be seen from Table I and Fig. 5 that the proposed MLE-MPPL method performs the best among the four methods.

C. Experiments on real data

To further verify the performance of the proposed MLE-MPPL, real spaceborne multipolarimetric data experiments are conducted. Thanks to the open access data policy of Sentinel-1A/B constellation mission, the (Pol)InSAR community has been constantly benefiting from its dual polarimetric data. Therefore, the dual polarimetric VV-VH Sentinel-1 data are employed here to validate our method. Specifically, 30 VV-VH Sentinel-1A Interferometric Wide swath SLC images acquired from 2017/12/10 to 2018/12/29 are selected here. Fig. 6(a) shows the spatial-temporal baseline distribution of the investigated images stack. The average temporal baseline between two neighboring acquisitions is about 12 days, and the test site is situated in Beijing, China. Fig. 6(b) shows the temporal averaged Pauli basis RGB images of the investigated scene. As marked by the red frames in Fig. 6(b), two regions of interest (ROIs), denoted as ROI-A and ROI-B, are examined. ROI-A has a size of 601×1401 and ROI-B's size is 501×1201. Their enlarged views are shown in Fig. 6(c) and 6(d), respectively. ROI-A is in Tongzhou district, Beijing, while ROI-B is in Beijing Capital International Airport.

Before performing phase series estimation, these SLCs are co-registered with respect to a common master image acquired at 2018/06/20 through the enhanced spectral diversity (ESD) method [45]. To reduce the impact of insufficient estimation of coherence matrix, the flat earth phase and topographic phase in each SLC are compensated using the 3 arcseconds digital elevation model (DEM) provided by the NASA SRTM mission. Figs. 6(g) and 6(h) show the original interferograms constructed by the 1st and 30th image acquisitions of VV channel in ROI-A and ROI-B, respectively. Evidently, the original VV interferograms of both ROIs have been severely contaminated by noise induced by the large temporal baseline of more than one year.

To achieve more accurate estimation of interferometric coherence matrix and separate PSs from DSs, a Kolmogorov-Smirnov (KS) test [11] with significance level $\alpha=0.05$ is applied to identify SHPs. Pixels with less than 8 SHPs inside a 11×11 local window are deemed as PSs, which are not processed in this article. The homogeneous test is applied on both VV and VH channels, and pixels that are identified as SHPs in both channels are finally accepted as SHPs. Figs. 6(e) and 6(f) show the maps of SHPs number of each pixel in ROI-A and ROI-B, respectively, where 96.31% and 96.90% of pixels are identified as DSs.

To quantitatively evaluate the performance of the proposed method on this Sentinel-1A dataset, the proposed Pol-detR is applied. In addition, pseudo coherence [42] is also introduced, which is defined as

$$\rho_\phi=\left|\frac{1}{M}\sum_{i=1}^{M}e^{j\phi_i}\right| \tag{43}$$

where M is the number of samples inside the pseudo coherence estimation window, and ϕ_i is the interferometric phase. ρ_ϕ reveals the spatial variance in a local window, thus reflecting the spatial phase smoothness and stability of interferograms. Larger pseudo coherence indicates better phase quality. As suggested in [42], the window size for pseudo coherence computation is set to be 7×7. Furthermore, the number of residue points [43] is employed as another metric for phase quality evaluation, as it can partially reflect the difficulty of the phase unwrapping step in subsequent MTInSAR processing and thereby affect the deformation estimation result. Thus, less residue points usually indicate less phase unwrapping errors and more accurate deformation estimation.

Four phase series estimation methods, i.e., EMI, ESPO, TP and MLE-MPPL are performed on ROI-A and ROI-B, respectively. EMI is only performed on the VV channel. After obtaining the estimated phase series of 30 image acquisitions, interferograms are constructed by the 1st and 30th acquisitions, which have the longest temporal baseline up to 384 days. Figs. 7 and 8 show the interferograms of ROI-A and ROI-B acquired by four methods, respectively. Compared to the original VV

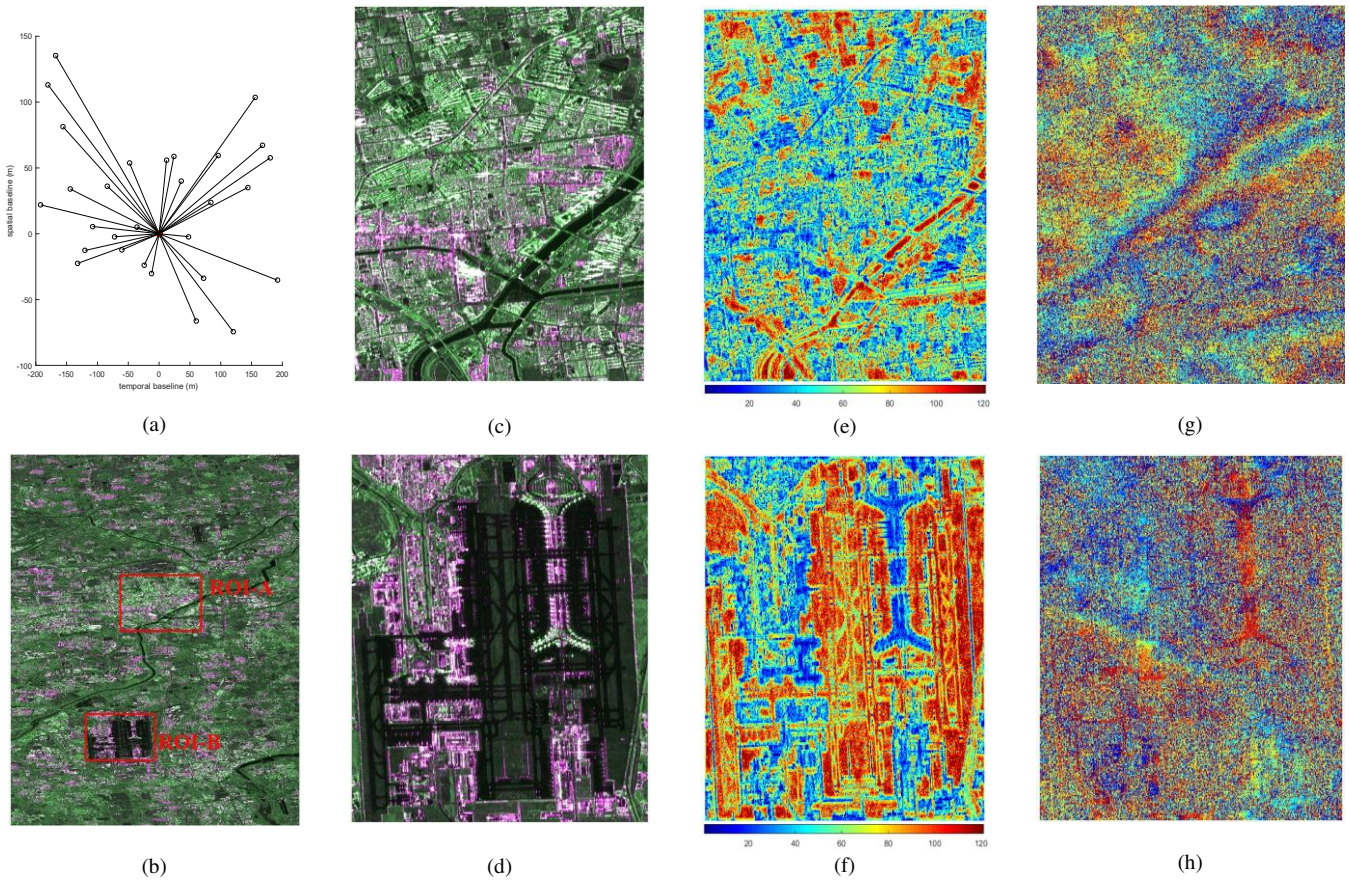

Fig. 6. Illustration of the investigated scene: (a) spatial-temporal baseline distribution of the investigated images stack; (b) PauliRGB images of whole investigated scene; (c) enlarged view of ROI-A; (d) enlarged view of ROI-B; (e) SHPs number map of ROI-A; (f) SHPs number map of ROI-B; (g) original VV interferogram of ROI-A constructed by the 1st and 30th acquisition; (h) original VV interferogram of ROI-B constructed by the 1st and 30th acquisition.

interferograms in Figs. 6(g) and 6(h), the noise in interferograms constructed from the estimated phase series by the four methods has been suppressed to certain extent. Further quantitative performance evaluation of the four methods is performed in terms of three metrics: residue points, pseudo coherence and Pol-detR respectively.

1) Pseudo coherence and residue points evaluation

The pseudo coherence distribution histograms for interferograms obtained by the four methods are shown in Fig. 9(a) and 9(b), and the corresponding average pseudo coherence values are listed in Table II. In addition, pixels with pseudo coherence $\rho_\phi \geq 0.6$ are defined as high-quality pixels. The number of high-quality pixels and residue points by each method is also shown in Table II.

From Figs. 9(a) and 9(b), it can be observed that the single polarimetric EMI histograms mainly concentrate on much lower values close to 0, and ESPO histograms are slightly better. On the other hand, TP and MLE-MPPL histograms are much more concentrated on higher values close to 1, while MLE-MPPL's histograms are the closest to 1. In Table II, it has also shown that MLE-MPPL has the highest average pseudo coherence value, the most high-quality pixels, and the least residue points. Clearly MLE-MPPL has achieved the best performance in terms of reduction of residues points and improvement of high-quality pixels at the same time.

It is also worth noting that in Table II, EMI has even more residue points in both ROI-A and ROI-B than the original VV. As EMI strongly depends on estimation accuracy of the magnitude of interferometric coherence matrix [46] [47], i.e., $\mathbf{\Gamma}$ in (2), a poor estimate of $\mathbf{\Gamma}$ will severely degrade EMI's phase-linking performance, resulting in more residue points, even than that of the original VV; whereas in the MLE-MPPL, $\mathbf{\Gamma}_{ESM}$ is estimated using three polarimetric channels, which significantly increases the number of looks and thereby improves the estimation accuracy.

2) Pol-detR evaluation

The average Pol-detR values of DSs by four methods in both ROIs are shown in Table III. It can be found that the proposed MLE-MPPL has the minimum average Pol-detR in both ROIs, which implies that it has the minimum average RMSE. To compare the Pol-detR performance of MLE-MPPL to other three methods on pixel basis, the pixel-based Pol-detR differences of MLE-MPPL with respect to EMI, ESPO and TP are computed as

$$\begin{aligned} \text{diff-EMI} &= \left(\text{Pol-detR}\right)_{EMI} - \left(\text{Pol-detR}\right)_{MLE-MPPL} \\ \text{diff-ESPO} &= \left(\text{Pol-detR}\right)_{ESPO} - \left(\text{Pol-detR}\right)_{MLE-MPPL} \\ \text{diff-TP} &= \left(\text{Pol-detR}\right)_{TP} - \left(\text{Pol-detR}\right)_{MLE-MPPL} \end{aligned} \tag{44}$$

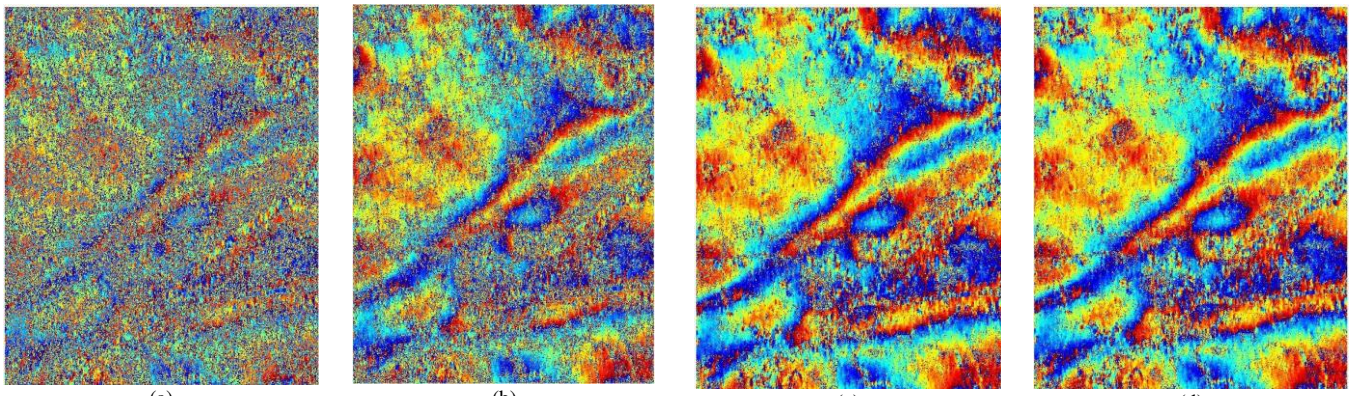

(a) (b) (c) (d)

Fig. 7. Interferograms constructed by the 1st and 30th acquisitions of each method in ROI-A: (a) EMI; (b) ESPO; (c) TP; (d)MLE-MPPL.

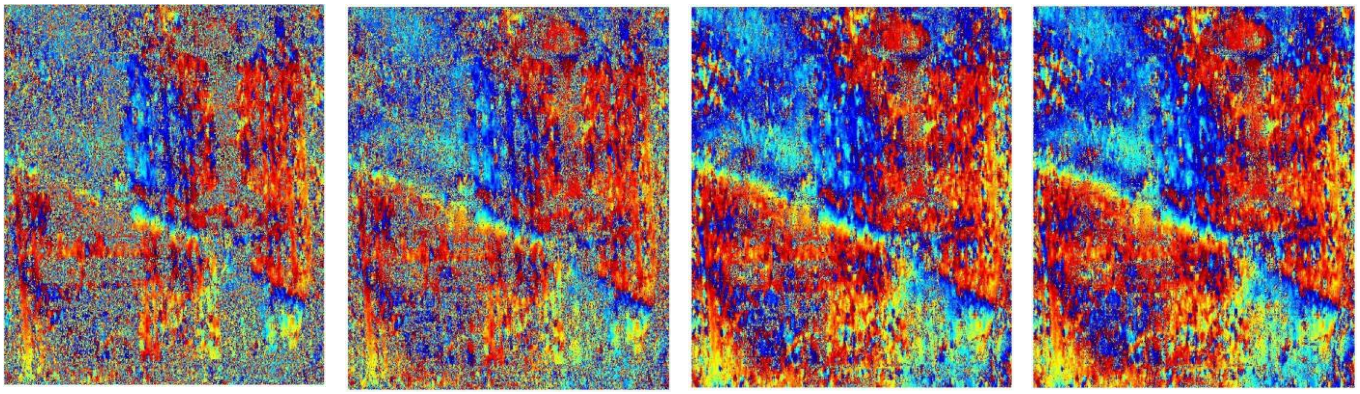

(a) (b) (c) (d)

Fig. 8. Interferograms constructed by the 1st and 30th acquisitions of each method in ROI-B: (a) EMI; (b) ESPO; (c) TP; (d)MLE-MPPL.

TABLE II
QUANTITATIVE EVALUATION OF PSEUDO COHERENCE PERFORMANCE BY FOUR METHODS

Method	Average pseudo coherence in ROI-A	Average pseudo coherence in ROI-B	High-quality pixels in ROI-A	High-quality pixels in ROI-B	Residue points in ROI-A	Residue points in ROI-B
Original VV	0.3201	0.2951	49813	37595	145782	115002
EMI	0.2788	0.4198	55526	170787	219022	119491
ESPO	0.4785	0.4830	285017	209145	149019	103901
TP	0.7080	0.6924	614802	413894	62632	44463
MLE-MPPL	**0.7352**	**0.7294**	**651718**	**453554**	**52077**	**34517**

For a certain pixel, a positive Pol-detR difference value indicates that MLE-MPPL has better Pol-detR performance than the other method on that pixel. The histograms of diff-EMI, diff-ESPO and diff-TP are shown in Fig. 10, where the y-axis in Fig. 10 has been transformed into logarithm for better visual inspection. It can be seen that the value of diff-EMI, diff-ESPO and diff-TP mostly concentrate on positive values. The ratios of positive value in diff-EMI, diff-ESPO and diff-TP are computed and shown in Table IV. It can be found that MLE-MPPL outperforms EMI, ESPO and TP on 85.81%, 91.82% and 72.59% pixels accordingly in ROI-A and on 86.54%, 91.73% and 64.22% pixels respectively in ROI-B.

3) Computational complexity comparison

As a rough indicator of the computational complexity of these four methods, their running time in both ROIs is recorded and listed in Table III. All experiments are conducted in MATLAB on a PC with 8-core Intel Core i7-8850H CPU and 16GB RAM environment.

As shown, the proposed MLE-MPPL takes more time than EMI and TP because it requires the additional sum of Kronecker product decomposition, but it is far more computationally efficient than ESPO.

V. CONCLUSIONS

In this work, a maximum likelihood estimator for multipolarimetric phase series estimation, MLE-MPPL, has been proposed and the corresponding CRLB derived, which is 1/3 of that for the single polarimetric scenario. An optimum solution for multipolarimetric phase series estimation is achieved with the minimum RMSE and it can asymptotically

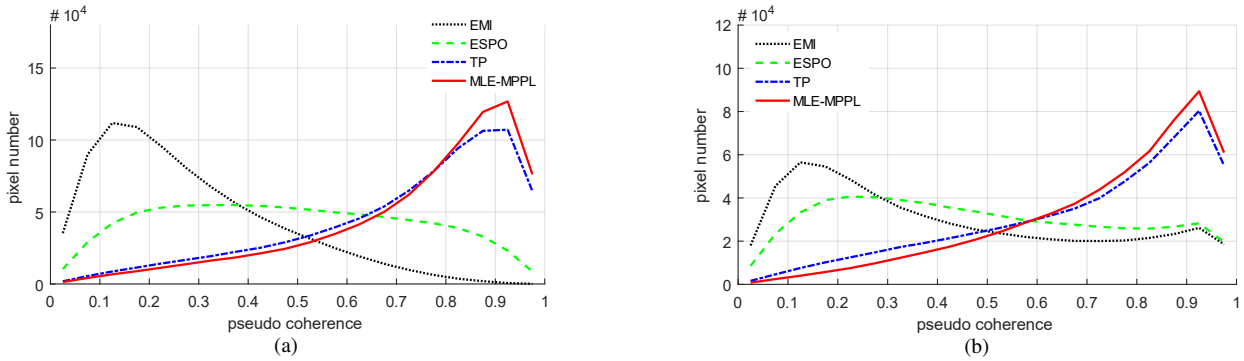

Fig. 9. Histograms of the pseudo coherence of four methods in two ROIs: (a) ROI-A; (b) ROI-B.

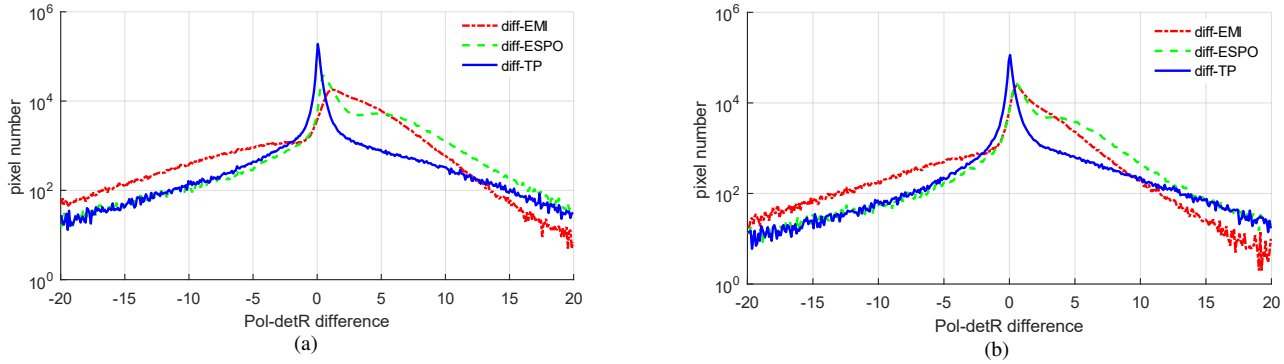

Fig. 10. Histograms of the diff-EMI, diff-ESPO and diff-TP in two ROIs: (a) ROI-A; (b) ROI-B.

TABLE III
AVERAGE POL-DETR VALUES AND RUNNING TIME OF FOUR METHODS

Method	Average Pol-detR in ROI-A	Average Pol-detR in ROI-B	Running time of ROI-A (hour)	Running time of ROI-B (hour)
EMI	-51.76	-32.82	0.6186	0.5251
ESPO	-51.04	-31.80	84.83	63.25
TP	-53.35	-33.62	1.087	0.9519
MLE-MPPL	**-53.73**	**-34.09**	9.351	7.701

TABLE IV
RATIO OF POSITIVE POL-DETR DIFFERENCE

Pol-detR difference	Ratio of positive value in ROI-A (%)	Ratio of positive value in ROI-B (%)
diff-EMI	85.81	86.54
diff-ESPO	91.82	91.73
diff-TP	72.59	64.22

reach the CRLB.A new metric called Pol-detR was proposed as an alternative to RMSE to evaluate the performance in multipolarimetric phase series estimation when the RMSE is not feasible in practice. As demonstrated by experiments based on both simulated and real data, the proposed MLE-MPPL has achieved the best performance among the considered solutions.

APPENDIX A

In this appendix, derivation of the MLE of $\mathbf{\Gamma}_{ESM}$ is elaborated in detail.

Using the trace property, $L_{pol}(\boldsymbol{\theta})$ in (26) can be transformed into

$$L_{pol}(\boldsymbol{\theta}) = -\sum_{i=1}^{3\times 3} \operatorname{trace}\left(\mathbf{C}_{pol}^{-1}\tilde{\mathbf{C}}_{pol,i}\right)\operatorname{trace}\left(\boldsymbol{\Theta}\tilde{\mathbf{C}}_{coh,i}\boldsymbol{\Theta}^{H}\mathbf{\Gamma}_{ESM}^{-1}\right) - 3\ln\det\left(\mathbf{\Gamma}_{ESM}\right) - N\ln\det\left(\mathbf{C}_{pol}\right) \tag{45}$$

For convenience of further analysis, we define an assistant variable

$$\mathbf{W}_i = \operatorname{Re}\left(\boldsymbol{\Theta}\tilde{\mathbf{C}}_{coh,i}\boldsymbol{\Theta}^{H}\right) \tag{46}$$

Since the logarithmic likelihood function $L_{pol}(\boldsymbol{\theta})$ and $\mathbf{\Gamma}_{ESM}$ are all real-valued, (45) can be transformed into

$$L_{pol}\left(\boldsymbol{\theta}\right)=-\sum_{i=1}^{3\times3}\operatorname{trace}\left(\mathbf{C}_{pol}^{-1}\tilde{\mathbf{C}}_{pol,i}\right)\operatorname{trace}\left(\mathbf{W}_i\boldsymbol{\Gamma}_{ESM}^{-1}\right)-3\ln\det\left(\boldsymbol{\Gamma}_{ESM}\right)-N\ln\det\left(\mathbf{C}_{pol}\right) \tag{47}$$

With (47), the Jacobian matrix of $L_{pol}\left(\boldsymbol{\theta}\right)$ with respect to $\boldsymbol{\Gamma}_{ESM}$ can be derived

$$\frac{\partial L_{pol}\left(\boldsymbol{\theta}\right)}{\partial\boldsymbol{\Gamma}_{ESM}^{T}}=\sum_{i=1}^{3\times3}\boldsymbol{\Gamma}_{ESM}^{-1}\left(\operatorname{trace}\left(\mathbf{C}_{pol}^{-1}\tilde{\mathbf{C}}_{pol,i}\right)\mathbf{W}_i\right)\boldsymbol{\Gamma}_{ESM}^{-1}-3\boldsymbol{\Gamma}_{ESM}^{-1} \tag{48}$$

A necessary condition for the maximum likelihood requires a zero Jacobian matrix, which means

$$\sum_{i=1}^{3\times3}\boldsymbol{\Gamma}_{ESM}^{-1}\left(\operatorname{trace}\left(\mathbf{C}_{pol}^{-1}\tilde{\mathbf{C}}_{pol,i}\right)\mathbf{W}_i\right)\boldsymbol{\Gamma}_{ESM}^{-1}-3\boldsymbol{\Gamma}_{ESM}^{-1}=\mathbf{0} \tag{49}$$

Thus, the MLE of $\boldsymbol{\Gamma}_{ESM}$ can be derived from (49)

$$\boldsymbol{\Gamma}_{MLE}=\frac{1}{3}\sum_{i=1}^{3\times3}\operatorname{trace}\left(\mathbf{C}_{pol}^{-1}\tilde{\mathbf{C}}_{pol,i}\right)\mathbf{W}_i \tag{50}$$

For a given solution of phase series estimation, $\boldsymbol{\Gamma}_{MLE}$ is

$$\boldsymbol{\Gamma}_{MLE}=\frac{1}{3}\sum_{i=1}^{3\times3}\operatorname{trace}\left(\mathbf{C}_{pol}^{-1}\tilde{\mathbf{C}}_{pol,i}\right)\operatorname{Re}\left(\hat{\boldsymbol{\Theta}}\tilde{\mathbf{C}}_{coh,i}\hat{\boldsymbol{\Theta}}^{H}\right) \tag{51}$$

REFERENCES

[1] Massonnet, D., Rossi, M., Carmona, C., Adragna, F., Peltzer, G., Feigl, K., Rabaute, T., "The displacement field of the Landers earthquake mapped by radar interferometry," *Nature*, 364 (6433), 138–142, 1993.

[2] Massonnet, D., Briole, P., Arnaud, A., "Deflation of Mount Etna monitored by spaceborne radar interferometry," *Nature*, 375, 567–570, 1995.

[3] Roberta Bonì, Massimiliano Bordoni, Alessio Colombo, Luca Lanteri, Claudia Meisina, "Landslide state of activity maps by combining multi-temporal A-DInSAR (LAMBDA)," *Remote Sensing of Environment*, vol. 217, pp.172-190, 2018.

[4] Jie Dong, Lu Zhang, Minggao Tang, Mingsheng Liao, Qiang Xu, Jianya Gong, Meng Ao, "Mapping landslide surface displacements with time series SAR interferometry by combining persistent and distributed scatterers: A case study of Jiaju landslide in Danba, China," *Remote Sensing of Environment*, vol. 205, pp. 180-198, 2018.

[5] Francesca Cigna, Deodato Tapete, "Satellite InSAR survey of structurally-controlled land subsidence due to groundwater exploitation in the Aguascalientes Valley, Mexico," *Remote Sensing of Environment*, vol. 254, 2021.

[6] A. Ferretti et al., "Submillimeter Accuracy of InSAR Time Series: Experimental Validation," *IEEE Transactions on Geoscience and Remote Sensing*, vol. 45, no. 5, pp. 1142-1153, May 2007.

[7] A. Ferretti, C. Prati and F. Rocca, "Nonlinear subsidence rate estimation using permanent scatterers in differential SAR interferometry," *IEEE Transactions on Geoscience and Remote Sensing*, vol. 38, no. 5, pp. 2202-2212, Sept. 2000.

[8] A. Ferretti, C. Prati, and F. Rocca, "Permanent scatterers in SAR interferometry," *IEEE Transactions on Geoscience and Remote Sensing*, vol. 38, pp. 2202–2212, Sept. 2000.

[9] O. Mora, J. J. Mallorqui and A. Broquetas, "Linear and nonlinear terrain deformation maps from a reduced set of interferometric SAR images," *IEEE Transactions on Geoscience and Remote Sensing*, vol. 41, no. 10, pp. 2243-2253, Oct. 2003.

[10] P. Berardino, G. Fornaro, R. Lanari and E. Sansosti, "A new algorithm for surface deformation monitoring based on small baseline differential SAR interferograms," *IEEE Transactions on Geoscience and Remote Sensing*, vol. 40, no. 11, pp. 2375-2383, Nov. 2002.

[11] A. Ferretti, A. Fumagalli, F. Novali, C. Prati, F. Rocca and A. Rucci, "A New Algorithm for Processing Interferometric Data-Stacks: SqueeSAR," *IEEE Transactions on Geoscience and Remote Sensing*, vol. 49, no. 9, pp. 3460-3470, Sept. 2011.

[12] G. Fornaro, S. Verde, D. Reale and A. Pauciullo, "CAESAR: An Approach Based on Covariance Matrix Decomposition to Improve Multibaseline–Multitemporal Interferometric SAR Processing," *IEEE Transactions on Geoscience and Remote Sensing*, vol. 53, no. 4, pp. 2050-2065, April 2015.

[13] N. Cao, H. Lee and H. C. Jung, "A Phase-Decomposition-Based PSInSAR Processing Method," *IEEE Transactions on Geoscience and Remote Sensing*, vol. 54, no. 2, pp. 1074-1090, Feb. 2016.

[14] H. Ansari, F. De Zan and R. Bamler, "Efficient Phase Estimation for Interferogram Stacks," *IEEE Transactions on Geoscience and Remote Sensing*, vol. 56, no. 7, pp. 4109-4125, July 2018.

[15] C. Wang et al., "A New Likelihood Function for Consistent Phase Series Estimation in Distributed Scatterer Interferometry," *IEEE Transactions on Geoscience and Remote Sensing*, vol. 60, pp. 1-14, 2022, Art no. 5227314.

[16] Hooper, A.; Zebker, H.; Segall, P.; Kampes, B., "A new method for measuring deformation on volcanoes and other natural terrains using InSAR persistent scatterers," *Geophysics Research Letters*. 31, L23661, 1–5, 2004.

[17] Kampes, B, *Radar Interferometry: Persistent Scatterer Technique*. Springer Publishing Company: The Netherlands, 2006.

[18] D. Perissin and T. Wang, "Repeat-Pass SAR Interferometry With Partially Coherent Targets," *IEEE Transactions on Geoscience and Remote Sensing*, vol. 50, no. 1, pp. 271-280, Jan. 2012.

[19] M. A. Siddique, U. Wegmüller, I. Hajnsek and O. Frey, "Single-Look SAR Tomography as an Add-On to PSI for Improved Deformation Analysis in Urban Areas," *IEEE Transactions on Geoscience and Remote Sensing*, vol. 54, no. 10, pp. 6119-6137, Oct. 2016.

[20] H. Ansari, F. De Zan and A. Parizzi, "Study of Systematic Bias in Measuring Surface Deformation With SAR Interferometry," *IEEE Transactions on Geoscience and Remote Sensing*, vol. 59, no. 2, pp. 1285-1301, Feb. 2021.

[21] F. De Zan, M. Zonno and P. López-Dekker, "Phase Inconsistencies and Multiple Scattering in SAR Interferometry," *IEEE Transactions on Geoscience and Remote Sensing*, vol. 53, no. 12, pp. 6608-6616, Dec. 2015.

[22] L. Pipia et al., "Polarimetric Differential SAR Interferometry: First Results with Ground-Based Measurements," *IEEE Geoscience and Remote Sensing Letters*, vol. 6, no. 1, pp. 167-171, Jan. 2009.

[23] V. D. Navarro-Sanchez and J. M. Lopez-Sanchez, "Improvement of persistent-scatterer interferometry performance by means of a polarimetric optimization," *IEEE Geoscience and Remote Sensing Letters*, vol. 9, no. 4, pp. 609–613, Jul. 2012.

[24] V. D. Navarro-Sanchez, J. M. Lopez-Sanchez and L. Ferro-Famil, "Polarimetric Approaches for Persistent Scatterers Interferometry," *IEEE Transactions on Geoscience and Remote Sensing*, vol. 52, no. 3, pp. 1667-1676, March 2014.

[25] L. Sagues, J. M. Lopez-Sanchez, J. Fortuny, X. Fabregas, A. Broquetas and A. J. Sieber, "Indoor experiments on polarimetric SAR interferometry," *IEEE Transactions on Geoscience and Remote Sensing*, vol. 38, no. 2, pp. 671-684, March 2000.

[26] R. Iglesias, D. Monells, X. Fabregas, J. J. Mallorqui, A. Aguasca and C. Lopez-Martinez, "Phase Quality Optimization in Polarimetric Differential SAR Interferometry," *IEEE Transactions on Geoscience and Remote Sensing*, vol. 52, no. 5, pp. 2875-2888, May 2014.

[27] F. Zhao and J. J. Mallorqui, "Coherency Matrix Decomposition-Based Polarimetric Persistent Scatterer Interferometry," *IEEE Transactions on Geoscience and Remote Sensing*, vol. 57, no. 10, pp. 7819-7831, Oct. 2019.

[28] F. Zhao and J. J. Mallorqui, "SMF-POLOPT: An Adaptive Multitemporal Pol(DIn)SAR Filtering and Phase Optimization Algorithm for PSI Applications," *IEEE Transactions on Geoscience and Remote Sensing*, vol. 57, no. 9, pp. 7135-7147, Sept. 2019.

[29] A. G. Mullissa, D. Perissin, V. A. Tolpekin and A. Stein, "Polarimetry-Based Distributed Scatterer Processing Method for PSI Applications," *IEEE Transactions on Geoscience and Remote Sensing*, vol. 56, no. 6, pp. 3371-3382, June 2018.

[30] Z. Sadeghi, M. J. Valadan Zoej, A. Hooper and J. M. Lopez-Sanchez, "A New Polarimetric Persistent Scatterer Interferometry Method Using Temporal Coherence Optimization," *IEEE Transactions on Geoscience and Remote Sensing*, vol. 56, no. 11, pp. 6547-6555, Nov. 2018.

[31] K. Ishitsuka, T. Matsuoka and M. Tamura, "Persistent Scatterer Selection Incorporating Polarimetric SAR Interferograms Based on Maximum Likelihood Theory," *IEEE Transactions on Geoscience and Remote Sensing*, vol. 55, no. 1, pp. 38-50, Jan. 2017.

[32] P. Shen, C. Wang, J. Hu, H. Fu and J. Zhu, "Interferometric Phase Optimization Based on PolInSAR Total Power Coherency Matrix Construction and Joint Polarization-Space Nonlocal Estimation," *IEEE Transactions on Geoscience and Remote Sensing*, vol. 60, pp. 1-14, 2022, Art no. 5201014.

[33] P. Shen et al., "A Novel Polarimetric PSI Method Using Trace Moment-Based Statistical Properties and Total Power Interferogram Construction," *IEEE Transactions on Geoscience and Remote Sensing*, vol. 60, pp. 1-15, 2022, Art no. 4402815.

[34] Shen, P., Wang, C., Hu, J., "A Polarization Stacking Method for Optimizing Time-Series Interferometric Phases of Distributed Scatterers," *Remote Sensing*, 14, 4168, 2022.

[35] Peng Shen, Changcheng Wang, Chihao Hu, Jun Hu, Haiqiang Fu, Jianjun Zhu, "JPPL: A joint-polarization phase linking algorithm for phase optimization of TSPolInSAR data," *International Journal of Applied Earth Observation and Geoinformation*, vol. 112, 102889, 2022.

[36] S. Tebaldini, "Algebraic Synthesis of Forest Scenarios From Multibaseline PolInSAR Data," *IEEE Transactions on Geoscience and Remote Sensing*, vol. 47, no. 12, pp. 4132-4142, Dec. 2009.

[37] C. Van Loan and N. Pitsianis, "Approximation with Kronecker products," *Linear Algebra for Large Scale and Real Time Applications*, M. S. Moonen, G. H. Golub, and B. L. R. De Moor, Eds. Norwell, MA: Kluwer, 1993, pp. 293–314.

[38] A. M. Guarnieri and S. Tebaldini, "Hybrid Cramer–Rao Bounds for Crustal Displacement Field Estimators in SAR Interferometry," *IEEE Signal Processing Letters*, vol. 14, no. 12, pp. 1012-1015, Dec. 2007.

[39] A. M. Guarnieri and S. Tebaldini, "On the Exploitation of Target Statistics for SAR Interferometry Applications," *IEEE Transactions on Geoscience and Remote Sensing*, vol. 46, no. 11, pp. 3436-3443, Nov. 2008.

[40] Van Trees, Harry L., *Optimum array processing: part iv of detection, estimation and modulation theory*. Wiley-Interscience.2002.

[41] J.-S. Lee, S. R. Cloude, K. P. Papathanassiou, M. R. Grunes, and I. H. Woodhouse, "Speckle filtering and coherence estimation of polarimetric SAR interferometry data for forest applications," *IEEE Transactions on Geoscience and Remote Sensing*, vol. 41, no. 10, pp. 2254–2263, Oct. 2003.

[42] M. Neumann, L. Ferro-Famil and A. Reigber, "Multibaseline Polarimetric SAR Interferometry Coherence Optimization," *IEEE Geoscience and Remote Sensing Letters*, vol. 5, no. 1, pp. 93-97, Jan. 2008.

[43] R. F. Hanssen, *Radar Interferometry: Data Interpretation and Error Analysis*. Dordrecht, The Netherlands: Kluwer, 2001.

[44] S. R. Cloude, *Polarisation: Applications in Remote Sensing*. New York, NY, USA: Oxford Univ. Press, 2009, ch. 3, pp. 115–177.

[45] R. Scheiber and A. Moreira, "Coregistration of interferometric SAR images using spectral diversity," *IEEE Transactions on Geoscience and Remote Sensing*, vol. 38, no. 5, pp. 2179-2191, Sept. 2000.

[46] S. Zwieback and F. J. Meyer, "Reliable InSAR Phase History Uncertainty Estimates," *IEEE Transactions on Geoscience and Remote Sensing*, vol. 60, pp. 1-9, 2022.

[47] S. Zwieback, "Cheap, Valid Regularizers for Improved Interferometric Phase Linking," *IEEE Geoscience and Remote Sensing Letters*, vol. 19, pp. 1-4, 2022.

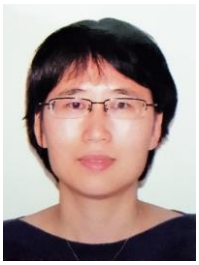

Huaping Xu received her B.S. degree in electronic engineering and Ph.D. degree in communication and information system from Beihang University in 1998 and 2003, respectively. She is currently a Professor with the School of Electronic and Information Engineering, Beihang University.

Her current research interests include synthetic aperture radar (SAR) interferometry, differential SAR interferometry, image processing and radar waveform design. She has now published more than 100 journal and conference papers, and a research monograph about signal processing.

Guobing Zeng received B.S. degree in Aircraft engineering from Beihang University, Beijing, China, in 2019. He is currently working towards the Ph.D. degree with the School of Electronic and Information Engineering at Beihang University.

His current research interests are in SAR interferometry, differential SAR interferometry and polarimetric differential SAR interferometry.

Wei Liu (S'01-M'04-SM'10) received his BSc and LLB. degrees from Peking University, China, in 1996 and 1997, respectively, MPhil from the University of Hong Kong in 2001, and PhD from the School of Electronics and Computer Science, University of Southampton, UK, in 2003. He then worked as a postdoc first at Southampton and later at the Department of Electrical and Electronic Engineering, Imperial College London. Since September 2005, he has been with the Department of Electronic and Electrical Engineering, University of Sheffield, UK, first as a Lecturer and then a Senior Lecturer. He has published about 350 journal and conference papers, five book chapters, and two research monographs titled "Wideband Beamforming: Concepts and Techniques" (John Wiley, March 2010) and "Low-Cost Smart Antennas" (by Wiley-IEEE, March 2019), respectively. His research interests cover a wide range of topics in signal processing, with a focus on sensor array signal processing and its various applications, such as robotics and autonomous systems, human computer interface, radar, sonar, satellite navigation, and wireless communications.

Yuan Wang received the B.S. degree in School of Information and Communication Engineering from Communication University of China, Beijing, China, in 2019. She is currently working towards the Ph.D. degree with the School of Electronic and Information Engineering at Beihang University.

Her current research interests include synthetic aperture radar (SAR) interferometry, and interferometric SAR image processing.